View Article Online
View Journal

Dalton Transactions

An international journal of inorganic chemistry

Accepted Manuscript

This article can be cited before page numbers have been issued, to do this please use: R. Bikas, E. Shahmoradi, S. Reinoso, M. Emami, L. Lezama, J. Sanchiz and N. Noshiranzadeh, *Dalton Trans.*, 2019, DOI: 10.1039/C9DT01652J.

ROYAL SOCIETY OF CHEMISTRY

rsc.li/dalton

View Article Online
DOI: 10.1039/C9DT01652J

Graphical Abstract

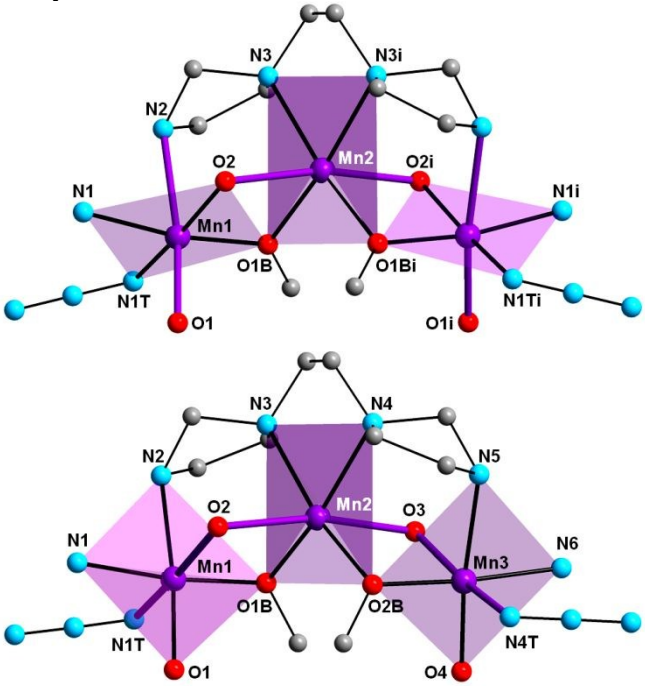

The effect of the orientation of the Jahn-Teller distortion on the magnetic interactions in two new mixed-valence trinuclear Mn(III)-Mn(II)-Mn(III) complexes have been investigated.

View Article Online
DOI: 10.1039/C9DT01652J

ARTICLE

The effect of the orientation of the Jahn-Teller distortion on the magnetic interactions of trinuclear mixed-valence Mn(II)/Mn(III) complexes

Received 00th January 20xx,

Accepted 00th January 20xx

DOI: 10.1039/x0xx00000x

Rahman Bikas,[*,a] Elaheh Shahmoradi,[b] Santiago Reinoso,[c] Marzieh Emami,[b] Luis Lezama,[d] Joaquín Sanchiz,[e] and Nader Noshiranzadeh[b]

Two new trinuclear manganese complexes, $[Mn_3(L^1)(\mu\text{-}OCH_3)_2(N_3)_2]\cdot CH_3OH$ (**1**) and $[Mn_3(L^2)(\mu\text{-}OCH_3)_2(N_3)_2]\cdot CH_3OH$ (**2**), have been obtained from the reaction of $Mn(OAc)_2\ 4H_2O$, NaN_3 and the preformed N_6O_4-donor H_4L^1 or H_4L^2 compartmental ligands, which are synthesized via Schiff base condensation of pentaethylenehexamine with 2-hydroxybenzaldehyde or 2-hydroxy-3-methoxybenzaldehye, respectively. Complexes **1** and **2** have been characterized by spectroscopic methods and single-crystal X-ray analysis. The structural studies indicate that both **1** and **2** are mixed-valence complexes containing angular Mn(III)–Mn(II)–Mn(III) cores in which the metal centers are connected to each other by phenoxido and methoxido bridging groups. The coordination environment around the manganese ions is analogous in both complexes, but for a change in the direction of the Jahn-Teller distortion around the external Mn(III) ions when going from **1** to **2**, which is mainly attributed to the steric effect of different substituents on the phenyl rings of the ligands. The analysis of the magnetic susceptibility data indicates the presence of antiferromagnetic intramolecular coupling in both complexes, but the interaction in **1** was found to be nearly one order of magnitude weaker than that in **2**. This fact is rationalized on the basis of the different orientation of the Jahn-Teller distortion, which modifies the magnetic exchange pathway through the phenoxido bridges from the *equatorial-axial* connection type observed in **1** to the *axial-axial* linkages displayed by **2**.

Introduction

The coordination chemistry of manganese continues to attract considerable scientific attention because of the numerous applications of Mn-based coordination compounds in a wide range of fields, including chemistry, biology, materials science, catalysis and physics.[1] Among such compounds, polynuclear mixed-valence manganese complexes have become a focus of great interest in recent years because they have been employed as effective biomimetic models for various biological systems and metalloenzymes containing Mn-based bioactive sites, such as the oxygen-evolving center of photosystem II,[2] superoxide dismutases,[3] ribonucleotide reductases[4] and catalases.[5] Mixed-valence manganese complexes are also interesting materials for electronic, spectroscopic, structural and theoretical investigations.[6]

Manganese has a variety of oxidation states and its multinuclear complexes can involve relevant electron transfer reactions.[7] In addition, most of manganese clusters possess large numbers of unpaired electrons, which makes them attractive precursors for magnetic studies. In molecular magnetism, mixed-valence manganese complexes stand out as one of the major species that can show single-molecule magnet (SMM) behavior and slow magnetization relaxation.[8] The presence of a combination of high ground-state spins and negative axial zero-field splitting parameter are the primary and main requirements for a molecule to function as a SMM.[9] Six-coordinated manganese(III) ions in near-octahedral geometry tend to display significant molecular anisotropy originating from the Jahn-Teller distortion that is usually observed in Mn(III) centers with high-spin d^4 electronic configuration.[10] In turn, manganese(II) ions with d^5 electronic configuration have the highest possible number of unpaired electrons in 3d orbitals. Thus, mixed-valence Mn(II)-Mn(III) complexes show the highest potential to behave as SMM, thereby representing ideal candidates to perform magnetic investigations.[11]

[a] *Department of Chemistry, Faculty of Science, Imam Khomeini International University, 34148-96818 Qazvin, Iran*
[b] *Department of Chemistry, Faculty of Science, University of Zanjan, 45371-38791 Zanjan, Iran*
[c] *Institute for Advanced Materials (InaMat), Universidad Pública de Navarra, Edificio Jerónimo de Ayanz, Campus de Arrosadia, 31006 Pamplona, Spain*
[d] *Departamento de Química Inorgánica, Facultad de Ciencia y Tecnología, Universidad del País Vasco UPV/EHU, P.O. Box 644, 48080 Bilbao, Spain*
[e] *Department of Chemistry, Faculty of Science, Instituto de Materiales y Nanotecnología, University of La Laguna, 38206 Tenerife, Spain*
* Corresponding Authors, Email addresses: Bikas_r@yahoo.com , Bikas@sci.ikiu.ac.ir (R. Bikas)

Electronic Supplementary Information (ESI) available: FT-IR (Fig. S1–S4) and UV-Vis (Fig. S5 and S6) spectra; additional figures for the structure of complex **1** (Fig. S7), the model of the magnetic exchange within the title complexes (Scheme S1), and the molecular orbitals of complex **2** (Fig. S8 and S9); additional tables for the bond angles (Table S1), the bond valence sum calculations (Tables S2 and S3), and the parameters of the magnetic fitting equations (Table S4) for the title complexes; and crystallographic CIF files for complexes **1** and **2**. See DOI: 10.1039/x0xx00000x

View Article Online
DOI: 10.1039/C9DT04653J

Structural parameters like the nature of bridging groups between metal ions, the metal···metal distances, or the metal-ligand bond lengths and angles are known to have significant influence on the nature and magnitude of magnetic interactions between metal ions in coordination clusters.[12] Moreover, the type of organic ligands and the specific coordination environment around the metal centers have also been confirmed to affect the magnetic properties in such clusters.[13] Therefore, the number of magneto-structural studies has significantly increased in recent years as several experimental and theoretical studies have been carried out to correlate how variations of these structural parameters affect the magnetic interactions.[14] The Jahn-Teller distortion is one of the most important structural parameters determining the observation of a special magnetic behavior like SMM. Despite the influence of the Jahn-Teller distortion on magnetic coupling having being thoroughly explored,[15] literature reports about the effect of its direction on the nature and magnitude of exchange magnetic interactions are still comparatively scarce. Undoubtedly, the direction of the Jahn-Teller distortion relative to the neighboring metal centers is a key structural parameter to be considered in magneto-structural studies, and trinuclear mixed-valence Mn(II)-Mn(III) complexes can be very useful models to perform such magneto-structural studies. Although modeling of their magnetic susceptibility data can render some difficulties,[16] such type of complexes offers efficacious simple models with small nuclearity for identifying the effect on the magnetic interactions of key structural parameters such as the direction of Jahn-Teller distortion.

In this study, we report the synthesis, crystal structure, spectroscopic properties and magnetic behavior of two new trinuclear mixed-valence Mn(III)-Mn(II)-Mn(III) complexes of general formula $[Mn_3(L)(\mu\text{-}OCH_3)_2(N_3)_2]\cdot CH_3OH$. The complexes have been prepared by using two new N_6O_4-donor Schiff base ligands (L) that are obtained from condensation of pentaethylenehexamine with 2-hydroxybenzaldehyde or 2-hydroxy-3-methoxybenzaldehye. Such compartmental ligands can simultaneously coordinate up to three metal ions and have high potential in stabilizing manganese in both Mn(II) and Mn(III) oxidation states. The direction of the Jahn-Teller distortion of the Mn(III) centers has been found to change as a function of the type of substituent on the phenyl rings, which makes the title complexes suitable compounds for studying the effects of such structural parameter on the exchange magnetic coupling interactions.

Results and discussion

Syntheses and spectroscopy

The multidentate N,O-donor Schiff base ligands were synthesized through the condensation of pentaethylenehexamine with 2-hydroxybenzaldehyde (H_4L^1) or 2-hydroxy-3-methoxybenzaldehyde (H_4L^2) in refluxing methanol (Scheme 1). The absence of any peak originating from stretching vibrations of N–H bonds in the FT-IR spectra of the ligands (Figs. S1–S2 in the ESI†) shows that all of the NH groups of the amine precursor are involved in the condensation reaction with the corresponding benzaldehyde derivative, in such a way that no NH group is left in the structure of the ligands. The trinuclear manganese complexes, **1** and **2**, were obtained from the reaction of $Mn(OAc)_2\cdot 4H_2O$, NaN_3 and the corresponding ligand (H_4L^1 or H_4L^2) in methanol. The appearance of a band at about 1615 cm^{-1} in the FT-IR spectra of the title complexes (Figs. S3–S4 in the ESI†) is assigned to the ν(C=N) vibration mode. This band is slightly red-shifted relative to that observed for the free ligands (ca. 1632 cm^{-1}), which is indicative of coordination to the metal ions through the azomethine nitrogen atoms as the formation of such M–N bonds weakens the C=N double bond.[17] The signal associated with the ν(C–O) stretching vibration is observed in the 1100–1300 cm^{-1} range, whereas a medium-to-weak metal-sensitive stretching band in the 440–406 cm^{-1} range can be assigned to the ν(Mn–N) vibration. Compared to the spectra of the free ligands, an additional new sharp peak of very strong intensity is observed at 2040 cm^{-1} for **1** and 2033 cm^{-1} for **2**. This band is assigned to the stretching vibration of the azide group and confirms the presence of terminal azide ligands in the structure of the title complexes.[18]

Figs. S5 and S6 in the ESI† display the electronic spectra of the free ligands and complexes **1** and **2**. For H_4L^1 and H_4L^2, the intense absorption bands in the region of 255-265 nm and 316-420 nm can be assigned to the $n\rightarrow\pi^*$ transitions of the imine and phenolic groups, respectively, whereas the higher energy band at 215 and 217 nm may be correlated to the $\pi\rightarrow\pi^*$ transitions. Such bands are shifted in the UV-Vis spectra of complexes **1** and **2** relative to the free ligands, and this fact indicates the coordination of the latter to the manganese ions. Moreover, the broad bands at lowest energies of 300-450 nm are due to ligand-to-metal charge transfer (LMCT) transitions.

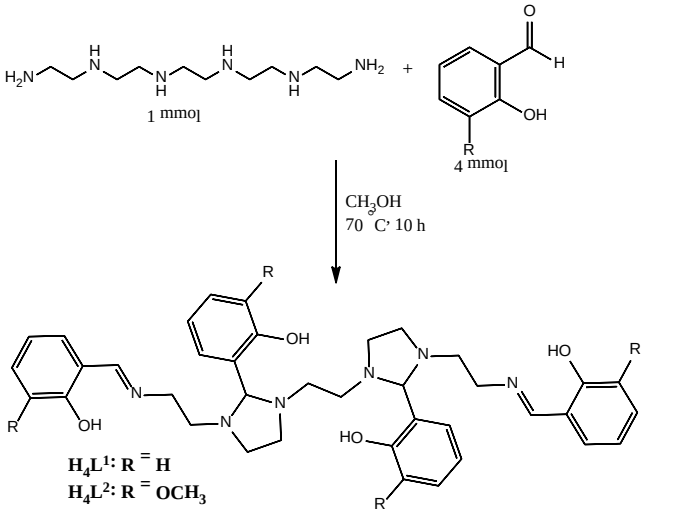

Scheme 1. Synthetic pathway and structure of the ligands H_4L^1 and H_4L^2.

X-ray structures of complexes 1 and 2

Single-crystal X-ray studies show that both **1** and **2** are very closely-related trinuclear neutral complexes in which one Schiff base ligand, two bridging methoxy groups, and two

terminal azide anions are involved in coordination to three manganese centers arranged in angular fashion (Fig. 1). The X-ray diffraction results confirm the proposed structure for the H_4L^1 and H_4L^2 ligands as they evidence that the external primary amine functionalities of the hexa-amine precursor have undergone Schiff base condensation, while the four central secondary amines have reacted with two aldehyde molecules to form two imidazolidine rings. In both complexes, the Schiff bases behave as tetra-negative decadentate ligands by supplying three N_2O_2-donor compartments defined by four phenolate oxygen, two azomethine nitrogen and four tertiary nitrogen atoms to coordinate the metal ions. The Schiff bases not only chelate the three manganese atoms, but also act as bridging ligands that connect neighboring metal centers through the oxygen atoms of the two central phenolate groups and the four nitrogen atoms of the two imidazolidine rings.

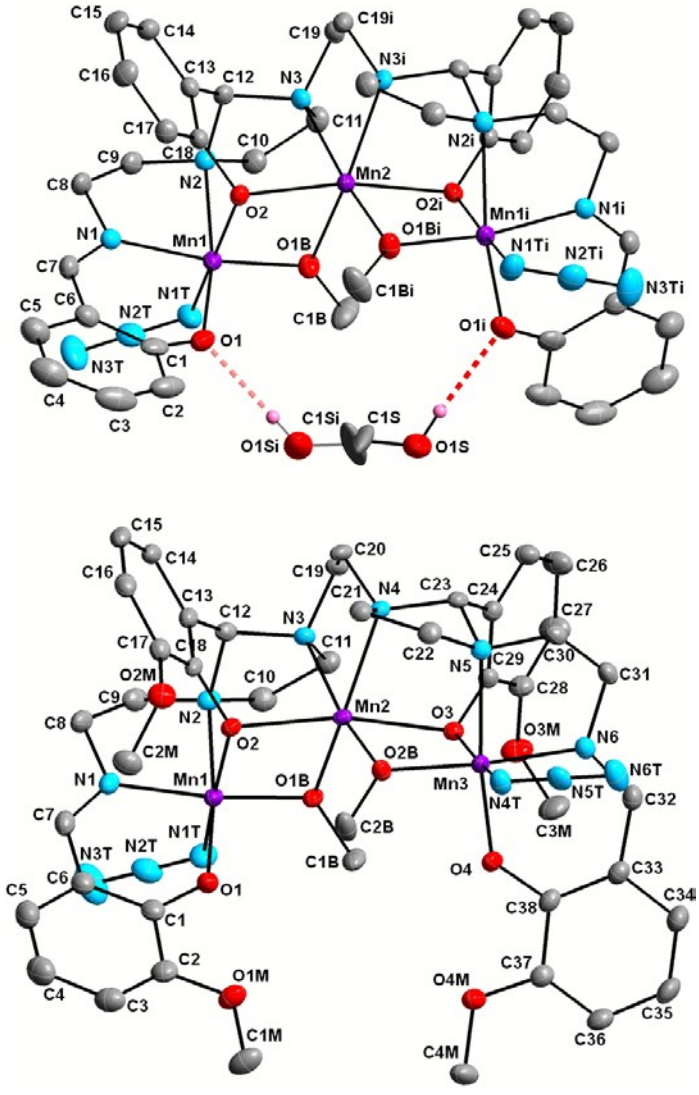

Fig. 1. ORTEP views (50% displacement ellipsoids) of the molecular structures of complexes **1** (top) and **2** (bottom) with atom labeling. Hydrogen atoms not involved in hydrogen-bonding interactions (dotted sticks) are omitted for clarity. The two positions over which the crystallization methanol molecule in **1** is disordered are represented in different colors for a better visualization, whereas the peripheral methanol molecule in **2** is not depicted. Symmetry code: i) $-x+2, y, -z+1/2$.

Compound **1** crystallizes in the monoclinic *C2/c* space group with the tri-manganese complex placed on a 2-fold rotation axis parallel to the crystallographic *b* axis that passes through the central metal atom (Mn2) and the middle of the C19–C19^i bond bridging the imidazolidine rings (Fig. S7 in the ESI†), and hence, the two outer manganese ions are crystallographically equivalent (Mn1 and Mn1^i). The methanol molecule of crystallization is located in the cleft defined by the two external phenolate branches and closely interacts with the phenolate oxygen atom O1^i through hydrogen bonding (O1S···O1^i = 2.807(4) Å, <O1S–H1S–O1^i> = 159(8)°). Since the carbon atom of this methanol of crystallization also lies on the 2-fold rotation axis, the solvent molecule results disordered over two half-occupied positions. In contrast, compound **2** crystallizes in the monoclinic $P2_1/n$ space group with the whole complex in general positions, that is, both the central (Mn2) and outer (Mn1 and Mn3) manganese centers are crystallographically independent. In this case, the steric hindrance imposed by the methoxy groups occupying *ortho*-positions in the phenolate rings hampers any solvent of crystallization from occupying the cleft in between the external phenolate branches as in compound **1**. Thus, the methanol molecule occupies a peripheral position and establishes a somewhat weaker hydrogen-bonding interaction with the outermost N atom of one of the terminal azide ligands instead of with a phenolate oxygen atom (O1S···N3T^{ii} = 2.882(4) Å, <O1S–H1S–N3T^{ii}> = 154(4)°; *ii* = $-x+3/2, y+1/2, -z+3/2$).

Selected bond lengths and intermetallic parameters for complexes **1** and **2** are listed in Table 1, whereas bond angles are compiled in Table S1 in the ESI†. In both cases, the three manganese centers are six-coordinated in distorted octahedral geometry, and the central Mn2 ion is linked by two μ_2-bridging oxygen atoms of one internal phenoxido group and one exogenous methoxido ligand to each of the two outer manganese atoms. The resulting corner-sharing, subtly bended Mn_2O_2 metallacycles display Mn2···Mn$_{outer}$ distances that range from 3.1056(4) in **1** to 3.1403(4) and 3.1438(4) Å in **2**, being the Mn$_{outer}$···Mn2···Mn$_{outer}$ angle slightly wider in **2** than in **1** (134.909(12) vs. 132.119(19)°) due to the presence of bulky methoxy substituents on the external phenolate rings. The Mn–O–Mn bond angles are in the 101.66(7)–104.35(6)° and 92.06(5)–95.88(6)° ranges for those involving the bridging methoxido (O1B and O2B) and phenoxido (O2 and O3) groups, respectively. The former Mn–O$_{OMe}$–Mn angles are about 2° wider in **2** than in **1**, whereas the reverse trend is observed for the latter Mn–O$_{OPh}$–Mn angles. The central Mn2 and the outer manganese ions can be unequivocally assigned as Mn(II) and Mn(III), respectively, on the basis of the bond lengths around these metal centers and the sum of eight negative charges provided by the ligands (four negative charges from the $(L^1)^{4-}$ or $(L^1)^{4-}$ Schiff bases, two negative charges from two terminal azide anions, and two negative charges from two exogenous methoxido ligands). The oxidation states determined for the Mn ions are also confirmed by bond valence sum calculations, which are summarized in Tables S2 and S3 in the ESI†. Therefore, both complexes are mixed-valence Mn(III)–(μ_2-O)$_2$–Mn(II)–(μ_2-O)$_2$–Mn(III) species with angular geometry.

View Article Online
DOI: 10.1039/C6DT01653J

View Article Online
DOI: 10.1039/C9DT01652J

Table 1. Selected bond lengths, intermetallic distances (Å), and intermetallic angles (°) for complexes **1** and **2**

Complex 1		Complex 2		
	100 K		100 K	293 K
		Bond Lengths		
Mn1—O1B	1.8748(16)	Mn1—O1B	1.8695(14)	1.8671(19)
Mn1—N1	2.0067(18)	Mn1—O1	1.8952(14)	1.892(2)
Mn1—O1	2.0322(18)	Mn1—N1	1.9829(17)	1.980(2)
Mn1—N1T	2.043(2)	Mn1—N2	2.1642(16)	2.170(2)
Mn1—O2	2.0460(15)	Mn1—O2	2.2118(13)	2.2184(18)
Mn1—N2	2.3156(18)	Mn1—N1T	2.2286(18)	2.216(3)
Mn2—O1B	2.1259(16)	Mn2—O1B	2.1021(13)	2.0987(18)
Mn2—O1B^{i}	2.1259(16)	Mn2—O2B	2.1174(13)	2.1254(19)
Mn2—O2	2.1361(14)	Mn2—O2	2.1512(14)	2.1424(19)
Mn2—O2^{i}	2.1361(14)	Mn2—O3	2.1527(13)	2.1533(19)
Mn2—N3	2.3419(18)	Mn2—N4	2.3247(15)	2.335(2)
Mn2—N3^{i}	2.3419(18)	Mn2—N3	2.3429(15)	2.369(2)
		Mn3—O2B	1.8762(14)	1.8706(19)
		Mn3—O4	1.8998(14)	1.900(2)
		Mn3—N6	1.9968(17)	1.992(2)
		Mn3—O3	2.1519(13)	2.1500(19)
		Mn3—N5	2.1966(15)	2.206(2)
		Mn3—N4T	2.2363(17)	2.239(3)
		Intermetallic Distances and Angles		
Mn1···Mn2	3.1056(4)	Mn1···Mn2	3.1403(4)	3.1498(6)
		Mn2···Mn3	3.1438(4)	3.1518(6)
Mn1^{i}···Mn2···Mn1	132.119(19)	Mn3···Mn2···Mn1	134.909(12)	135.671(17)

Symmetry code: *i*) −*x*+2, *y*, −*z*+1/2.

The central Mn(II) ion displays in both complexes a distorted octahedral MnO_4N_2 coordination environment defined by two phenolate oxygen atoms at the axial positions and an equatorial plane formed by two oxygen atoms from the bridging methoxido ligands and two inner nitrogen atoms provided by the imidazolidine rings. In this equatorial plane, two oxygen atoms, as well as two nitrogen atoms, are located at *cis*-related positions with respect to each other. The Mn–O and Mn–N bond lengths around Mn2 are close to those observed for other Mn(II) complexes reported in literature.[19] The peripheral Mn(III) ions show distorted octahedral MnO_3N_3 environments with the coordination sites occupied by two oxygen atoms from one external (O1, O4) and one bridging (O2, O3) phenolate groups, another oxygen atom from a bridging exogenous methoxido ligand (O1B, O2B), one azomethine nitrogen atom (N1, N6), and another two nitrogen atoms from one imidazolidine ring (N2, N5) and one terminal azide ligand (N1T, N4T).

Close inspection of the bond lengths around these outer metal centers reveals significant differences in the orientation of their coordination polyhedra. For complex **1**, the Mn1–N2 bond (2.3156(18) Å) is significantly longer than the remaining Mn–N and Mn–O bonds (equal or shorter than 2.0460(15) Å), and therefore, this nitrogen atom of the imidazolidine ring together with the *trans*-related oxygen atom of the external phenolate group would occupy the axial positions according to the Z-out Jahn-Teller effect that is usually found in most octahedral Mn(III) centers with high spin d^4 configuration.[20] This fact would result in an equatorial plane formed by the *cis*-related pair of azomethine/azide nitrogen atoms and the *cis*-related pair of bridging methoxy/phenoxy oxygen atoms. Thus, the connectivity between the outer Mn(III) and central Mn(II) ions in complex **1** would be of the type *equatorial-equatorial* through the bridging methoxido ligand and *equatorial-axial* through the bridging phenoxido group (Fig. 2).

In the case of **2**, the longest bond for both crystallographically independent Mn(III) centers is that involving the nitrogen atom from the terminal azide ligand (Mn1–N1T and Mn3–N4T) instead of the imidazolidine group. Therefore, the direction along which the Z-out Jahn-Teller distortion takes place is modified relative to complex **1**, in such a way that the equatorial planes of the Mn(III) centers in **2** would be defined by the pair of azomethine/imidazolidine nitrogen atoms and the oxygen atoms from the bridging methoxido ligand and the external phenoxido group, while the axial coordination sites would be occupied by the azide ligand and the *trans*-related bridging phenolate group. This change in the direction of the Jahn-Teller distortion is evidenced upon comparison of the short Mn(III)–N_{azide} and bridging Mn(III)–O_{OPh} bond lengths in complex **1** (2.043(2) and 2.0460(15) Å) with those lengthened in **2** (2.2286(18) and 2.2118(13) Å for Mn1, 2.2363(17) and 2.1519(13) Å for Mn3). This change induces also the slightly longer Mn2···Mn_{outer} distances observed in complex **2** relative to **1** due to the Jahn-Teller elongation taking place along the phenolate bridging groups. As a consequence, the connectivity between the outer Mn(III) and central Mn(II) ions is also partially modified: while the *equatorial-equatorial* linkage through the bridging methoxido ligands is maintained, the connection through the bridging phenoxido groups goes from *equatorial-axial* in **1** to the *axial-axial* type observed for

complex **2** (Fig. 2). This fact can be attributed to the steric effects associated with the methoxy groups occupying *ortho*-positions in the phenolate rings of complex **2**. The $-OCH_3$ substituents of the external phenolate branches display the usual nearly coplanar arrangement, but those on the central phenolate groups are bended towards the external phenolates forming angles of ca. 35° with the aromatic rings to which they are bonded, in such a way that the Mn(III)–(μ_2-O)$_2$–Mn(II)–(μ_2-O)$_2$–Mn(III) backbone of **2** undergoes slight distortions to accommodate such central $-OCH_3$ functionalities (elongation along the N_{azide}–Mn(III)–O_{OPh} axes and opening of the Mn(III)–O_{OMe}–Mn(II) angles). It is also worth noting the fact that the crystallization methanol molecule forms O–H···O_{OPh} or O–H···N_{azide} hydrogen bonds with ligands coordinated to axial positions of the Mn(III) ions in both **1** and **2**. Such hydrogen bonding interactions might also be an effective parameter in changing the direction of the Jahn-Teller distortion in these complexes.

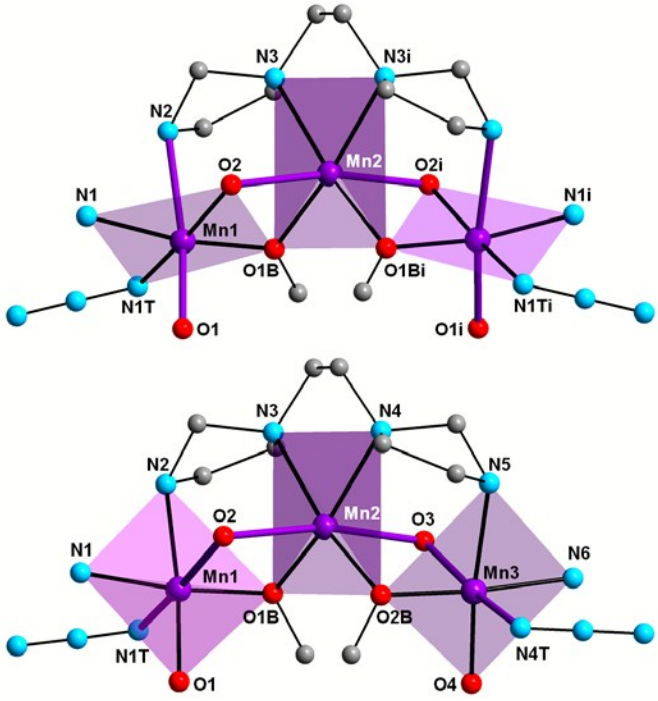

Fig. 2. Detail of the coordination environments around the manganese centers highlighting the different relative orientations of equatorial planes (translucent violet rectangles) and axial directions (violet sticks) found in the structures of complexes **1** (top) and **2** (bottom).

Magnetic properties

Fig. 3a shows the thermal evolution of the magnetic molar susceptibility (χ_m) and the $\chi_m T$ product for complexes **1** and **2** in the 2–300 K range. In both cases, the χ_m curve undergoes a continuous increase as the temperature decreases, reaching values up to 3.06 cm^3·mol^{-1} for **1** and 0.95 cm^3·mol^{-1} for **2** at 2 K. The susceptibility data are well described by the Curie-Weiss law in the 30–250 K range (insets in Fig. 3a). The calculated Curie constants (C) and Weiss temperatures (θ) are as follows: C = 10.45 cm^3·K·mol^{-1} and θ = –1.1 K for **1**, and C = 10.65 cm^3·K·mol^{-1} and θ = –8.6 K for **2**. These negative values of θ suggest the presence of dominant antiferromagnetic (AF) interactions in both complexes, and this observation is consistent with the overall shape of the $\chi_m T$ vs T curve.

View Article Online
DOI: 10.1039/C6DT01653J

At room temperature, the experimental value of the $\chi_m T$ product is nearly the same for both complexes, 10.35 and 10.19 cm^3·K·mol^{-1} for **1** and **2**, respectively. These values are in good agreement with that of 10.37 cm^3·K·mol^{-1} expected for a $Mn^{III}_2Mn^{II}$ system made of magnetically isolated high-spin ions with g = 2.00 when considering Mn^{III} (S = 2) and Mn^{II} (S = 5/2) spin-only contributions of 3.00 and 4.37 cm^3·K·mol^{-1}, respectively. For complex **1**, the $\chi_m T$ vs T curve remains nearly constant upon cooling to temperatures around 70 K, below which it decreases smoothly down to ca. 20 K and drops at lower temperatures to reach a value of 6.11 cm^3·K·mol^{-1} at 2K. In the case of **2**, this decrease of the $\chi_m T$ vs T curve starts taking place at higher temperatures (ca. 150 K) and shows a more gradual nature. The final drop below ca. 50 K results significantly more pronounced, in such a way that a much lower $\chi_m T$ value of only 1.94 cm^3·K·mol^{-1} is obtained at 2K. Both final $\chi_m T$ values are above 1.87 cm^3·K·mol^{-1}, which would correspond to a magnetically isolated Mn^{III}–Mn^{II}–Mn^{III} trimer with S = 3/2 ground state (g = 2.00). This behavior further supports the consideration of weak intratrimeric AF coupling accompanied with negligible intertrimeric interactions operating in both systems, and moreover, it also indicates that the magnetic exchange in **2** must be substantially stronger than that displayed by **1**.

It is worth noting at this point that a subtle anomaly consisting in a slight increase of $\chi_m T$ as the temperature lowers is observed for both $\chi_m T$ vs T curves at high temperatures (T > 250 K). This anomalous behavior is best defined for complex **2** and must be associated with a weakening of the AF coupling, which usually originates from changes in the bonding scheme around the metal centers in response to the thermal stimulus. To explore whether any crystalline phase transition or other structural modifications take place in the 250–300 K range, we performed an additional single-crystal X-ray diffraction measurement of **2** at room temperature. As shown in the Experimental Section (Table 3), both the cell symmetry and cell parameters determined at 100 K are retained for the room-temperature measurement, hence the occurrence of a phase transition can be ruled out. The geometric parameters around the manganese centers are also preserved nearly intact with negligible changes of only ca. 0.01 Å in the bond lengths or interatomic distances and ca. 1° in the bond angles as the most significant variations (Table 1 and Table S1 in the ESI†). Thus, this high-temperature anomaly in the $\chi_m T$ vs T curves does not appear to associate with any structural feature, but its origin remains unclear to our knowledge.

The magnetic data have been first fitted using the isotropic spin exchange coupling model for trinuclear complexes (Model 1, illustrated with Scheme S1 in the ESI†). The Hamiltonian corresponding to this model can be expressed as $H = -2(J_{12}S_1S_2 + J_{23}S_2S_3 + J_{13}S_1S_3)$ where J_{ij} are the exchange coupling constants between the manganese ions i and j, and S_i represent the corresponding spin states.

View Article Online
DOI: 10.1039/C9DT01652J

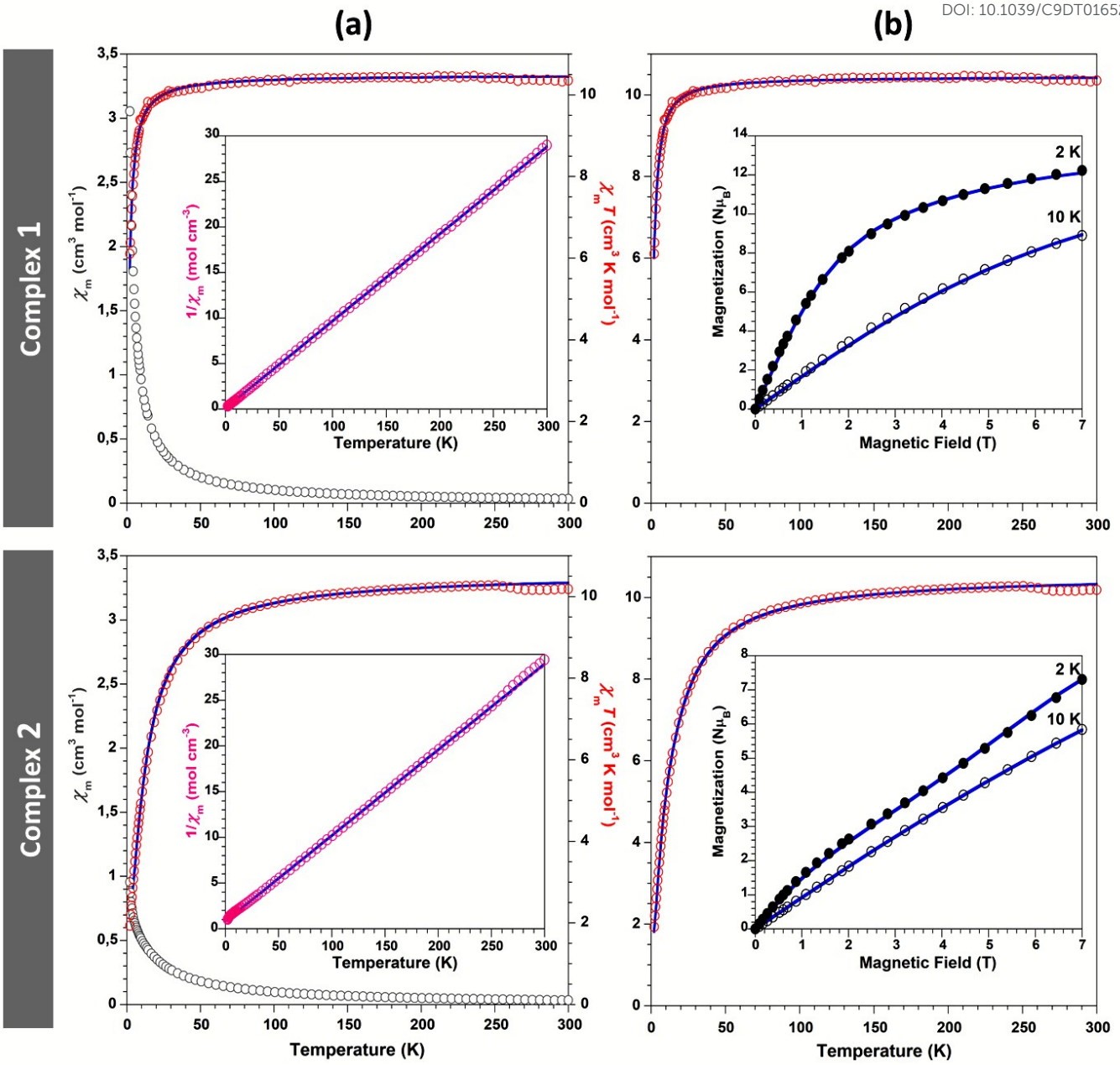

Fig. 3. (a) Thermal dependence of the magnetic molar susceptibility (χ_m, gray circles) and the $\chi_m T$ product (red circles) of complexes **1** and **2**, and best fit obtained from Model 1 (solid blue line); (b) Best fit of the $X_m T$ vs T curves (red circles, static field of 0.1 T) obtained from Model 2 (solid blue line). Insets: (a) thermal dependence of $1/\chi_m$ (pink circles) and best fit to the Curie-Weiss expression (solid blue line); (b) field-dependent magnetization curves at 2 (black circles) and 10 K (hollow circles) and best fit obtained from Model 2 (solid blue line).

In our case, we have made the following considerations: (1) in spite of the angular nature of the title complexes, the through-space interaction between the two outermost Mn(III) ions is expected to be nonexistent due to the long intermetallic distances (Mn1···Mn1^{i} = 5.6768(5) Å for **1**, Mn1···Mn3 = 5.8038(4) Å for **2**), and therefore, the third term in the Hamiltonian can be neglected (J_{13} = 0); (2) the two outermost Mn(III) ions in **1** are crystallographically equivalent due to the complex being located on a 2-fold rotation axis, and therefore, J_{12} must be equal to J_{23} in this system; (3) although not related by any symmetry element, the two outermost Mn(III) ions in **2** display nearly equivalent coordination environments and connectivity towards the central Mn(II) atom in terms of bond lengths/angles, and therefore, we can assume similar exchange interactions between these ions (J_{12} = J_{23}). These considerations simplify the Hamiltonian to $H = -2J(S_1S_2 + S_2S_3)$ for both complexes **1** and **2**. An analytical expression of the energy levels as a function of J for all of the spin states of the trimers can be obtained by applying the Kambe method.[21] This expression is $E_i = -J[S_T(S_T + 1) - S^*(S^* + 1) - S_2(S_2 + 1)]$, where $S^* = S_1 + S_3$ and $S_T = S^* + S_2$, and can be related with χ_m through the van Vleck equation. This fact leads to a second expression,

$\chi_m T = [Ng^2\mu_B{}^2k^{-1}][\Sigma a_i \exp(-E_i/kT)][\Sigma b_i \exp(-E_i/kT)]^{-1}$ (Equation 1), where N is the Avogadro's number, μ_B is the Bohr magneton, k is the Boltzmann constant, and g accounts for the average Landé factor. The values of the coefficients a_i and b_i, as well as those of the energy E_i as a function of J, are listed in Table S4 in the ESI† for all of the spin states of a Mn^{III}–Mn^{II}–Mn^{III} trinuclear complex. This procedure has been previously developed by Coronado and coworkers and satisfactorily applied to describe the magnetic properties of a large series of oxalate-bridged M^{III}–M^{II}–M^{III} trinuclear complexes with M^{III} = Cr, Fe and M^{II} = Mn, Fe, Ni, Cu.[22]

As shown in Fig. 3a, the experimental $\chi_m T$ vs T curves are very well reproduced by Model 1 in the whole temperature range with an overall weak AF exchange. The values of the exchange coupling constant and Landé factor afforded by the best fit of Equation 1 to the magnetic data are listed in Table 2. These values fully support our previous consideration of the AF coupling in complex **2** being much stronger than that operating in **1** (by nearly one order of magnitude). Moreover, they also compare well with the results obtained for other alkoxo-, phenoxo- and/or carboxylate-bridged Mn^{III}–Mn^{II}–Mn^{III} mixed-valence complexes in the literature,[23] which all show weak magnetic coupling of either ferromagnetic (F) or AF character ($-7.0 < J < 3.9$ cm^{-1}).

Table 2. Best fit results of the magnetic data of complexes **1** and **2**.

	Complex 1		Complex 2	
	Model 1	Model 2	Model 1	Model 2
J (cm^{-1})	–0.12	–0.10	–0.74	–0.72
g	2.01	2.007	2.02	2.018
D (cm^{-1})	–	–2.3	–	–10.2
R[a]	4.8×10^{-4}	0.122	6.4×10^{-4}	0.028

[a] For Model 2, the total residual is calculated as the product of the individual sum of squares errors for each data set (χ_m and M), for the different error scales of the individual data sets not obscuring any features.

Despite having proven its validity for analyzing M^{III}–M^{II}–M^{III} trinuclear complexes,[22] Model 1 might be considered as oversimplified for treating the magnetic data of **1** and **2**. Therefore, we decided to collect additional magnetization (M) data to perform a simultaneous fit of $\chi_m T$ vs T and M vs H curves that could confirm the results afforded by Model 1, as well as evaluate any potential influence of the zero-field splitting (ZFS) of Mn(III) ions on the magnetic behavior of **1** and **2**. For the largest magnetic field applied (7 T), the M values do not reach that expected for the saturation of a system consisting of two Mn(III) and one Mn(II) isolated ions (ca. 13 μN_B) for any of the two complexes at any of the temperatures analyzed. Moreover, the M values corresponding to complex **2** are in all cases substantially lower than those afforded by **1** (Fig. 4). The linear variation of M observed for the highest values of the applied magnetic field indicates that the title complexes do not show well-isolated ground states, not even at the lowest temperature of 2 K. The clear separation displayed by the isofield M vs H/T curves, which is noticeably more pronounced in the case of **2**, confirms this observation. This behavior could be due to the influence of the magnetic exchange interactions, but taking into account the weakness of the overall AF coupling and the presence of Mn(III) atoms involving significant Jahn-Teller distortion, it most likely originates mainly from a ZFS effect of the latter ions.

View Article Online
DOI: 10.1039/C6DT04653J

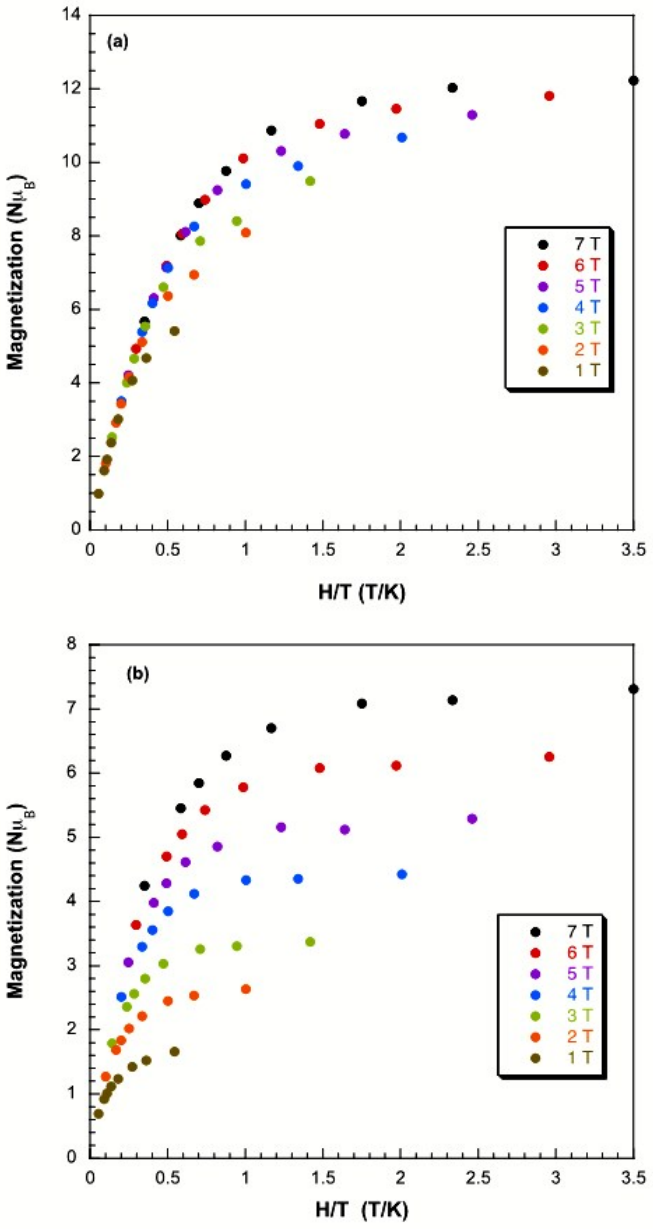

Fig. 4. Field and temperature-dependent magnetization curves for complexes **1** (top) and **2** (bottom) measured at applied fields in the 0–7.0 T range and at temperatures in the 2–20 K range.

The simultaneous fit of $\chi_m T$ vs T and M vs H curves at two different temperatures (2 and 10 K) has been carried out through the Hamiltonian $H = -2J(S_1S_2 + S_2S_3) + 2D_{Mn(III)}S_z^2$, where D accounts for the ZFS value of the Mn(III) ions (Model 2). The use of this Hamiltonian involves the following assumptions to avoid over-parametrization of the magnetic fit: (1) the parameter D is the same for the two Mn(III) ions in each complex (such ions are crystallographically equivalent for **1** and display virtually identical coordination environments for

View Article Online
DOI: 10.1039/C9DT01653J

2) and negligible for the Mn(II) centers; (2) the parameter *g* is isotropic and common to all manganese atoms of both complexes. The magnetic data have been treated with the program PHI,[24] which afforded the values of the *J*, *g*, and *D* parameters that are displayed in Table 2 as the best fit results.

The results obtained from applying Model 2 reproduce satisfactorily the evolution of χ_m and *M* with the temperature and the applied magnetic field, respectively (Fig. 3b). The values of the parameters *J* and *g* are consistent with those obtained from Equation 1. The absolute value of the parameter *D* results reasonable for complex **1**, but somewhat too high for **2** when compared to what reported in the literature for Mn(III) coordination systems.[25] In complex **2**, $|D|$ might be overestimated due to *J* and *D* being strongly correlated, but can be lowered to more usual values slightly below 3 cm^{-1} without significant impact on *J*, nor in the agreement factor *R*. For example, a value of $D = -3.00$ cm^{-1} would slightly strengthen *J* to -0.75 cm^{-1} and the fit to the experimental magnetic data would still be acceptable with a *R* factor of 0.145. This value is worse than that of the fit depicted in Fig. 3b, but still comparable to the *R* factor listed in Table 2 for complex **1**. The parameter *J* is mainly defined by the shape of the $\chi_m T$ vs *T* curve, so that the decrease of the latter upon cooling can only be reproduced by using absolute *J* values higher than 0.50 cm^{-1} in the case of **2**. These results confirm our previous observation of the AF coupling in complex **2** being much stronger than that operating in **1**. Moreover, they also indicate that the ZFS of the Mn(III) ions follows an analogous trend, being significantly larger for those in complex **2**.

The large number of singly occupied orbitals, the occurrence of interactions through different σ and π exchange pathways, and the variety of bridges found in the few examples of mixed-valence Mn^{III}–Mn^{II}–Mn^{III} complexes available has yet made impossible to establish clear magnetostructural correlations for these systems. Nevertheless, Kou and coworkers have pointed out on the basis of experimental results that the AF exchange should tend to weaken as the M–O(alkoxo)–M and M–O(phenoxo)–M bridging angles widen, in such a way that they tentatively conclude that M–O(alkoxo)–M angles larger than 102° should result in F coupling.[23c] In our case, the M–O(alkoxo)–M angle for **1** is nearly 102° (<Mn1–O1B–Mn2> = 101.66(7)°), which would be consistent with the very weak AF interaction observed for this complex. The introduction of –OMe substituents in the phenolate groups of the Schiff base ligand of **2** leads to a slight widening of the M–O(alkoxo)–M angles by ca. 2° (<Mn1–O1B–Mn2> = 104.35(6)° and <Mn2–O2B–Mn3> = 103.69(6)°) and to a subtle lengthening of the $Mn^{III}\cdots Mn^{II}$ distances (Table 1). This is accompanied by a significant shift of the methyl groups of the bridging methoxides out of the mean plane of the corresponding Mn_2O_2 metallacycles, which has been demonstrated to lower the overlap between the orbitals of the paramagnetic centers and those of the bridge[26] (τ = 10.89(12)° for **1** versus τ = 37.95(10) and 34.81(10)° for **2**, being τ the angle formed between the C–O bond of the bridging methoxide and the mean plane of the Mn_2O_2 metallacycle). All of these features suggest that the magnetic interaction through the *equatorial-equatorial* M–O(alkoxo)–M exchange pathway should weaken and most likely become of F nature when going from complex **1** to complex **2**. However, a significant strengthening of the overall AF interaction is experimentally observed instead. The fact that the M–O(phenoxo)–M angles become narrower by less than 4° when going from complex **1** (<Mn1–O2–Mn2> = 95.88(6)°) to complex **2** (<Mn1–O2–Mn2> = 92.06(5)° and <Mn2–O3–Mn3 = 93.83(5)°) could well counteract the weakening effect through the O(alkoxo) bridge by strengthening the AF coupling through this pathway. However, this contribution does not appear sufficient for reinforcing the overall AF interaction by one order of magnitude as observed for **2**, and therefore, this reinforcement should mainly be attributed to the change of the nature of the M–O(phenoxo)–M exchange pathway from an *equatorial-axial* linkage to an *axial-axial* one as a result of the structural distortions introduced by the –OMe substituents.

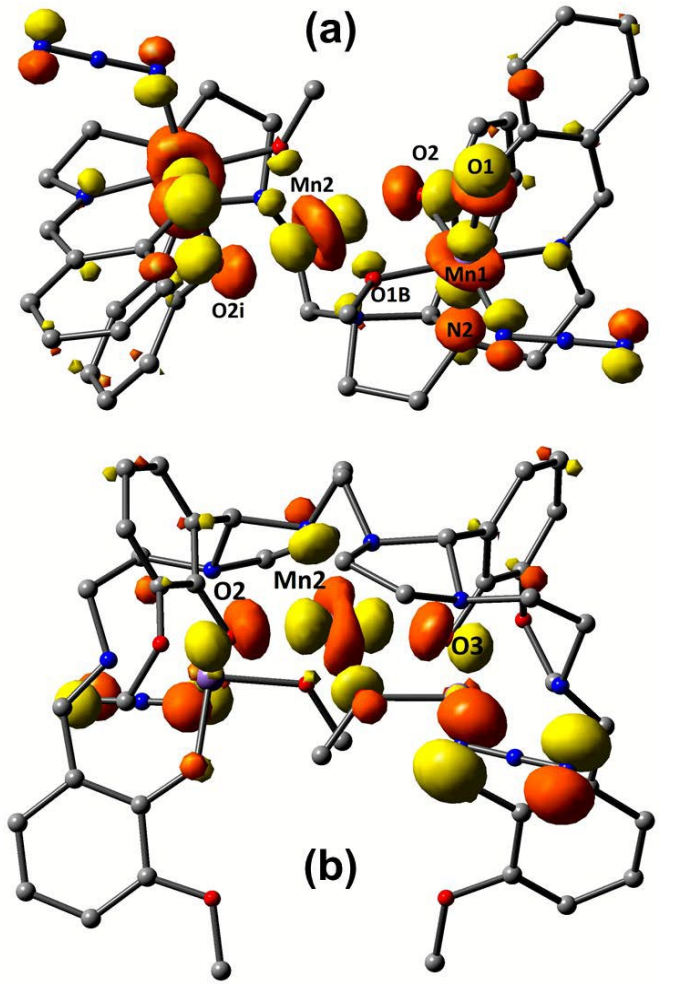

Fig. 5. (a) Surface plot of the HOMO for complex **1**, which contains the three d_{z^2} atomic orbitals of the Mn atoms and defines the z axis for each ion; (b) Surface plot of the d_{z^2} centered molecular orbital of Mn2 for complex **2**. Hydrogen atoms are omitted for clarity.

DFT Calculations

In order to obtain the relative orientation of the molecular orbitals of the Mn(II) and Mn(III) ions, DFT calculations were carried out on the experimental X-ray structures of **1** and **2**.

Fig. 5a shows the Highest Occupied Molecular Orbital (HOMO) of complex **1**, which contains the d_{z^2} orbitals of the three Mn atoms. The Z axis for the outermost, crystallographically equivalent Mn(III) ions (Mn1 and Mn1^{i}) is given by the orientation of the lobules of the d_{z^2} orbitals, which point towards the imidazolidine N2 and the phenoxido O1 atoms, whereas the orientation of the toroid defines the XY plane containing the azide N1T, bridging methoxido O1B, bridging phenoxido O2 and azomethine N1 atoms (omitted from the HOMO representation for clarity, see Fig. 2 for the atom labeling). At the same time, O2 and the crystallographically equivalent O2^{i} are the atoms filling the Z-axial positions for the central Mn(II) ion (Mn2). Therefore, the surface plot demonstrates that the bridging phenoxido O2 atom connects the *axial* position of Mn2 with an *equatorial* position of Mn1, while the bridging methoxido O1B connects in turn *equatorial* positions of both ions. Similarly, the calculations performed for complex **2** also results in phenoxido bridging oxygen atoms (O2 and O3) occupying the Z-axial positions of the central Mn2 ion (Fig. 5b). Moreover, and according to the surface plots of the d_{z^2}-centered molecular orbitals of Mn1 and Mn3 displayed in Figs. S8 and S9 in the ESI†, the coordination environments of these two Mn(III) centers show the same relative orientation to that schematized in Fig. 2. Therefore, such surface plots confirm the fact that the bridging methoxido and phenoxido oxygen atoms lead to *equatorial-equatorial* and *axial-axial* connections, respectively, as derived from the analysis of the structural parameters.

Conclusions

Two new trinuclear mixed valence Mn(III)-Mn(II)-Mn(III) angular complexes with general formula $[Mn_3(L)(\mu\text{-}OCH_3)_2(N_3)_2]\cdot CH_3OH$ have been synthesized and characterized by spectroscopic methods and single-crystal X-ray analysis. The complexes have been prepared by using two new compartmental N_6O_4-donor ligands (L) that are obtained from Schiff base condensation of pentaethylenehexamine with 2-hydroxybenzaldehyde (complex **1**) or 2-hydroxy-3-methoxybenzaldehye (complex **2**). Structural studies indicate that the coordination environment of metal ions is analogous in both complexes, but for a change in the direction of the Jahn-Teller distortion around the external Mn(III) ions when going from **1** to **2** that is most likely induced by the presence of bulky methoxy substituents on the phenyl rings of the ligand L in the latter complex. The analysis of the magnetic behavior in the range of 2-300 K indicates the presence of antiferromagnetic intramolecular interactions between metal ions in both complexes. The magnetic coupling in **2** proved to be nearly one order of magnitude stronger than that found in **1** despite the longer metal···metal distances, which has been attributed to the change in the orientation of the Jahn-Teller distortion modifying the magnetic exchange pathway through the phenoxido bridges from the *equatorial-axial* connection type observed in **1** to the *axial-axial* linkages shown by **2**.

Experimental

View Article Online
DOI: 10.1039/C9DT01652J

Materials and instrumentations

Manganese(II) acetate tetrahydrate, 2-hydroxybenzaldehyde, 2-hydroxy-3-methoxybenzaldehyde and pentaethylene-hexamine were purchased from Aldrich and used as received. Solvents of the highest commercially available grade were used without further purification. The FT-IR spectra were recorded as KBr disks on a Bruker TENSOR 27 FT–IR spectrophotometer. The solution UV–Vis spectra were recorded on a thermo-spectronic Helios Alpha spectrophotometer between 200 and 800 nm. The elemental analyses (carbon, hydrogen and nitrogen) were obtained from a Carlo ERBA Model EA 1108 analyzer. The manganese content of the complexes was determined by atomic absorption analysis on a Varian Spectra AA-220 equipment. The ^{1}H– and ^{13}C–NMR spectra of the ligands in $CDCl_3$ solution were measured on a Bruker Avance spectrometer operating at 250 and 62.9 MHz, respectively, and the chemical shifts (δ) are indicated in ppm relative to tetramethylsilane (TMS).

Synthesis of 2,2'-{ethane-1,2-diylbis[3-(2-{[(1*E*)-(2-hydroxyphenyl)methylene]amino}ethyl)imidazolidine-1,2-diyl]}diphenol (H_4L^1)

The ligand H_4L^1 was prepared by refluxing a mixture of 2-hydroxybenzaldehyde (1.27 ml, 12.00 mmol) and pentaethylenehexamine (0.73 ml, 3.00 mmol) in methanol (20 ml). The reaction mixture was heated to reflux for 10 h and the resulting yellow solid product was filtered off, washed successively with few amounts of cold ethanol and ether, and finally dried in air. Yield: 80.1% based on 2-hydroxybenzaldehyde (1.56 g). M.p. 148-151 ˚C. Anal. Calc. for $C_{38}H_{44}N_6O_4$ (MW = 648.79 g mol^{-1}): C, 70.35; H, 6.84; N, 12.95%; Found: C, 70.29; H, 6.87; N, 12.99%. FT-IR (KBr, cm^{-1}): 3427 (w, br), 2930 (m), 2815 (m), 1632 (vs), 1583 (m), 1495 (m), 1460 (m), 1414 (w), 1378 (w), 1340 (w), 1279 (s), 1263 (m), 1279 (w), 1152 (m), 1119 (w), 1031 (m), 972 (w), 889 (w), 848 (w), 757 (vs), 741 (m), 662 (w), 642 (w), 565 (w), 554 (w), 460 (w). ^{1}H–NMR (250 MHz, $CDCl_3$, 25 °C, TMS): δ = 2.02-2.24, 2.53-2.61, 2.71-2.74, 2.86-2.90, 3.71-3.41, 3.54-3.72 (all m, $20H_{aliphatic}$), 5.26 (s, 2H), 6.77-7.26 (m, $14H_{aromatic}$), 8.21 (s, 2H, $2H_{azomethine}$), 10.65 (broad, 2H, OH), 13.23 (broad, 2H, OH) ppm. ^{13}C–NMR (62.90 MHz, $CDCl_3$, 25 °C, TMS): δ = 165.9, 161.1, 158.4, 132.2, 131.4, 130.9, 130.8, 130.1, 121.1, 120.8, 118.7, 118.5, 116.9, 89.1, 58.3, 57.8, 55.5, 52.8, 50.9, 49.9, 49.8, 49.54, 49.2 ppm. UV-Vis (CH_3OH, c = 2.5×10^{-5} M, λ_{max} [nm] with ε [M^{-1} cm^{-1}]): 215 (49200), 255 (21900), 316 (6200).

Synthesis of 6,6'-((E)-3,3'-(ethane-1,2-diyl)bis(1-(2-((E)-(2-hydroxy-3-methoxybenzylidene)amino)ethyl)imidazolidine-3,2-diyl))bis(2-methoxyphenol) (H_4L^2)

The ligand H_4L^2 was prepared following a procedure similar to that used for H_4L^1, except for the fact that 2-hydroxy-3-methoxybenzaldehyde (1.83 g, 12.00 mmol) was used instead of 2-hydroxybenzaldehyde. H_4L^2 was obtained as a yellow viscose oil, which was washed several times with *n*-hexane and dichloromethane. The final product was obtained as a yellow

View Article Online DOI: 10.1039/C9DT04585E

powder after rotary evaporation of the remaining materials. Yield: 75% based on 2-hydroxy-3-methoxybenzaldehyde (1.73 g). Anal. Calc. for $C_{42}H_{52}N_6O_8$ (MW = 768.91 g mol^{-1}): C, 65.61; H, 6.82; N, 10.93%; Found: C, 65.52; H, 6.87; N, 10.99%. FT-IR (KBr, cm^{-1}): 3450 (w, br), 2925 (m), 2851 (m), 2818 (m), 1662 (w), 1632 (vs), 1583 (m), 1489 (m), 1460 (m), 1414 (m), 1383 (w), 1375 (w), 1341 (w), 1279 (s), 1263 (m), 1031 (m), 1151 (m), 1117 (w), 1032 (w), 1010 (w), 972 (w), 882 (w), 851 (w), 756 (vs), 737 (m), 668 (w), 642 (w), 556 (w), 454 (w). ^{1}H–NMR (250 MHz, $CDCl_3$, 25 °C, TMS): δ = 2.38-2.58, 3.37-3.57 (all m, $20H_{aliphatic}$), 3.86 (s, 12H, $4OCH_3$) 5.61 (s, 2H), 6.64-7.34 (m, $12H_{aromatic}$), 8.23 (s, $2H_{azomethine}$), 11.09 (broad, 2H, OH), 13.75 (broad, 2H, OH) ppm. ^{13}C–NMR (62.90 MHz, $CDCl_3$, 25 °C, TMS): δ = 166.1, 151.9,148.1, 124.45, 123.0, 121.2, 119.71, 118.1, 117.81, 13.8, 112.3, 111.4, 102.1, 89.34, 58.2, 56.0, 53.1, 52.7, 51.1, 49.7, 47.546.0 ppm. UV-Vis (CH_3OH, c = 2.5×10^{-5} M, λ_{max} [nm] with ε [M^{-1} cm^{-1}]): 217 (53000), 265 (19000), 420 (4900).

Synthesis of the complex $[Mn_3(L^1)(\mu\text{-}OCH_3)_2(N_3)_2]\cdot CH_3OH$ (1)

The ligand H_4L^1 (0.649 g, 1.000 mmol), $Mn(OAc)_2$ $4H_2O$ (0.980 g, 4.000 mmol) and NaN_3 (0.260 g, 4.000 mmol) were refluxed in methanol (30 ml) for 6 h under air atmosphere. The reaction mixture was left to cool down to room temperature and filtered to remove any undissolved residue. The filtrate was kept in an open reaction tube at ambient temperature and dark red crystals were obtained by slow evaporation after a few days. The crystals were separated from the mother liquors and washed with methanol. Yield: 63.48% based on H_4L^1 (0.627 g). Anal. Calc. for $C_{41}H_{50}Mn_3N_{12}O_7$ (MW = 987.75 g mol^{-1}): C, 49.86; H, 5.10; N, 17.02; Mn, 16.69%; Found: C, 49.78; H, 5.08; N, 17.11; Mn, 16.61%. FT-IR (KBr, cm^{-1}): 3421 (w, br), 2953 (w), 2922 (m), 2853 (m), 2813 (w), 2040 (vs), 1615 (vs), 1597 (m), 1567 (w), 1535 (w), 1525 (w), 1509 (w), 1482 (s), 1451 (m), 1442 (m), 1400 (w), 1385 (w), 1335 (w), 1311 (w), 1289 (m), 1200 (w), 1149 (w), 1095 (w), 1046 (m), 1032 (m), 995 (w), 964 (w), 928 (w), 907 (w), 894 (w), 855 (w), 796 (w), 761 (w), 745 (m), 669 (w), 638 (w), 610 (w), 583 (m), 522 (m), 504 (m), 490 (w), 469 (w),460 (w), 418 (w). UV-Vis (CH_3OH, c = 2.5×10^{-5} M, λ_{max} [nm] with ε [M^{-1} cm^{-1}]): 234 (75500), 276(42600), 405 nm (7160).

Synthesis of the complex $[Mn_3(L^2)(\mu\text{-}OCH_3)_2(N_3)_2]\cdot CH_3OH$ (2)

Complex **2** was synthesized by reacting H_4L^2 (0.769 g, 1.000 mmol), $Mn(OAc)_2$ $4H_2O$ (0.980 g, 4.000 mmol) and NaN_3 (0.260 g, 4.000 mmol) under the same conditions reported for complex **1**. Dark brown crystals were obtained upon slow solvent evaporation for one week, separated from the mother liquors and washed with cold methanol. Yield: 71.49% based on H_4L^2 (0.792 g). Anal. Calc. for $C_{45}H_{58}Mn_3N_{12}O_{11}$ (MW = 1107.85 g mol^{-1}): C, 48.79; H, 5.28; N, 15.17; Mn, 14.88%; Found: C, 48.72; H, 5.23; N, 15.26; Mn, 14.93%. FT-IR (KBr, cm^{-1}): 3438 (m, br), 2998 (w), 2922 (m), 2856 (w), 2813 (w), 2033 (vs), 1614 (s),1546 (m), 1483 (m), 1466 (m), 1448 (m), 1408 (w), 1390 (w), 1336 (w), 1313 (m), 1280 (s), 1243 (m), 1218 (w), 1194 (w), 1171 (w), 1134 (w), 1094 (w), 1077 (m), 1056 (m), 1031 (m), 1000 (w), 987 (w), 972 (w), 951 (w), 915 (w), 896 (m), 795 (w), 765 (m), 741 (m), 621 (w), 615 (w), 589 (w), 566 (w), 545 (w), 528 (m), 434 (w). UV-Vis (CH_3OH, c = 2.5×10^{-5} M, λ_{max} [nm] with ε [M^{-1} cm^{-1}]): 207 (56800), 234 (26000), 290 (11200), 328 nm (7450).

Magnetic studies

The magnetic measurements were performed on a Quantum Design MPMS3 Superconducting Quantum Interference Device (SQUID) magnetometer. The magnetic susceptibility data were collected between 2 and 300 K with an applied field of 0.1 T. The experimental susceptibilities were corrected for the diamagnetism of the constituent atoms by using Pascal tables. The magnetization measurements were performed at different temperatures between 2 and 20 K and the data were collected under applied magnetic fields ranging from 0 to 7 T.

X-ray crystallography

A summary of the crystal data and refinement details for complexes **1** and **2** is given in Table 3. The intensity data collection was performed on an Agilent Technologies SuperNova diffractometer equipped with mirror-monochromated Cu $K\alpha$ radiation (λ = 1.54184 Å) and Atlas CCD detector. The measurements were carried out using the ω-scan method at a temperature of 100(2) K controlled with an Oxford Cryosystems open-flow nitrogen cryostat. An additional data collection at 293(2) K was also carried out for complex **2**, but the SuperNova diffractometer was equipped with Mo $K\alpha$ radiation (λ = 0.71073 Å) and Eos CCD detector in this case. The data collections, unit cell refinements, data reductions, and corrections for Lorentz and polarization effects were performed with the CrysAlis^{Pro} software package.[27] This software was also used to apply routine multi-scan absorption corrections to the data. The structures were solved by direct methods using OLEX2,[28] and refined by full-matrix least squares on F^2 with SHELXL-97.[29] The refinement included anisotropic thermal parameters for all non-H atoms. All H-atoms were found in difference Fourier maps. In the final refinement cycles, the C-bonded H atoms were repositioned to their calculated positions and refined using a riding model with C–H bond lengths restrained to the standard values of 0.95 Å (aromatic C–H), 0.98 Å (methylic C–H), 0.99 Å (methylenic C–H) or 1.00 Å (methinic C–H). The thermal parameters were U_{iso}(H) = 1.2U_{eq}(C) for all hydrogen atoms except for those belonging to the methyl groups, for which thermal parameters of U_{iso}(H) = 1.5U_{eq}(C) were used. The O-bonded H atoms were refined with the O–H bond length restrained to 0.84(2) Å and a thermal parameter of U_{iso}(H) = 1.5U_{eq}(O) in all cases but for that in the room-temperature structure of **2**, which was placed in a calculated position and treated with a standard riding model (O–H = 0.82 Å, U_{iso}(H) = 1.5U_{eq}(O)) involving the refinement of the torsion angle from electron density. CCDC 1908371 (**1**), 1908372 (**2** at 100 K), and 1908373 (**2** at 293 K) contain the supplementary crystallographic for this article. These data can be obtained free of charge from The Cambridge Crystallographic Data Centre via www.ccdc.cam.ac.uk/structures.

View Article Online
DOI: 10.1039/C9DT01652J

Table 3. Crystallographic data and refinement details for compounds **1** and **2**

	Complex 1	**Complex 2**	
Formula	$C_{41}H_{50}Mn_3N_{12}O_7$	$C_{45}H_{58}Mn_3N_{12}O_{11}$	
M_r/g mol^{-1}	987.75	1107.85	
Crystal shape, color	block, dark red	plate, brown	
Crystal size/mm^3	0.17 × 0.12 ×0.11	0.37×0.11×0.05	0.52×0.21×0.11
T/K	100(2)	100(2)	293(2)
λ/Å	1.54184 (Cu Kα)	1.54184(Cu Kα)	0.71073(Mo Kα)
Device	SuperNova Atlas CCD	SuperNova Atlas CCD	SuperNova Eos CCD
Crystal system	Monoclinic	Monoclinic	Monoclinic
Space group	$C2/c$	$P2_1/n$	$P2_1/n$
a/Å	14.5962(4)	13.06284(12)	13.1976(3)
b/Å	17.2040(4)	27.2891(3)	27.4846(6)
c/Å	17.6348(5)	13.51506(11)	13.6058(3)
β/°	109.876(3)	92.8012(8)	93.0647(18)
V/Å^3	4164.53(19)	4812.00(8)	4928.19(18)
Z	4	4	4
D_{calc}/g cm^{-3}	1.575	1.529	1.493
μ/mm^{-1}	7.849	6.925	0.828
F(000)	2044	2300	2300
ϑ range/°	4.1–71.0	3.2–71.0	2.7–25.2
h,k,l	−17→17, −17→21, −21→21	−16→14, −31→33, −16→16	−12→15, −32→32, −16→16
R_{int}	0.054	0.043	0.039
$R(F)_{obs}$	0.036	0.032	0.043
$R_w(F^2)_{all}$	0.096	0.079	0.100
S	1.029	1.034	1.087
Abs. correction	multi-scan	multi-scan	multi-scan
Hydrogen refinement	mixed	mixed	constr
Measured reflect.	16569	44120	38440
Independent reflec.	4013	9291	8915
Reflect. with $I > 2\sigma(I)$	3567	8291	7321
Parameters	299	650	648
Restraints	1	1	0

DFT Calculations

Spin-unrestricted DFT calculations were performed at the B3LYP level by means of the Gaussian 09 code[30] with a triple-Z Gaussian basis set for the Mn atoms; 631-g for C, N and O; and 321-g for the H atoms. Single-point energy calculations without any optimization were performed by using the atomic positions taken from the CIF files of compounds **1** and **2**. The surface plots of the molecular orbitals were obtained with the Gauss View 5.0 visor. Hydrogen atoms have been omitted in the pictures for a better visualization.

Conflicts of interest

There are no conflicts to declare.

Acknowledgements

The authors are grateful to Imam Khomeini International University and the University of Zanjan for the financial support of this study. S.R. thanks Obra Social la Caixa, Fundación Caja Navarra and Universidad Pública de Navarra for a research contract in the framework of the program "Captación del Talento". Technical and human support provided by SGIker (UPV/EHU) is gratefully acknowledged.

Notes and references

1 (a) S. Paul, F. Neese and D. A. Pantazis, *Green Chem.*, 2017, **19**, 2309-2325; (b) M. Wiechen, H.-M. Berends and P. Kurz, *Dalton Trans.*, 2012, **41**, 21-31; (c) N. Niccolai, E. Tiezzi and G. Valensin, *Chem. Rev.*, 1982, **82**, 359–384; (d) K. F. Sibbons, K. Shastri and M. Watkinson, *Dalton Trans.*, 2006, 645-661; (e) M. M. Najafpour, G. Renger, M. Hołyńska, A. N. Moghaddam, E.-M. Aro, R. Carpentier, H. Nishihara, J. J. Eaton-Rye, J.-R. Shen and S. I. Allakhverdiev, *Chem. Rev.*, 2016, **116**, 2886–2936; (f) M. Grau, F. Rigodanza, A. J. P. White, A. Sorarù, M. Carraro, M. Bonchio and G. J. P. Britovsek, *Chem. Commun.*, 2014, **50**, 4607-4609; (g) S. Das, K. Khatua, A. Rakshit, A. Carmona, A. Sarkar, S. Bakthavatsalam, R. Ortega and A. Datta, *Dalton Trans.*, 2019, **48**, 7047-7061.

2 (a) M. M. Najafpour, *Dalton Trans.*, 2011, **40**, 3793-3795; (b) Z. Wei, C. W. Cady, G. W. Brudvig and H. J. M. Hou, *J. Photochem. Photobiol. B*, 2011, **104**, 118-125; (c) X. Li, D. P.

Kessissoglou, M. L. Kirk, V. L. Pecoraro and C. J. Bender, *Inorg. Chem.*, 1988, **27**, 1–3; (d) S. G. Mitchell, P. I. Molina, S. Khanra, H. N. Miras, A. Prescimone, G. J. T. Cooper, R. S. Winter, E. K. Brechin, D.-L. Long, R. J. Cogdell and L. Cronin, *Angew. Chem. Int. Ed.*, 2011, **50**, 9154-9157; (e) V. Krewald, M. Retegan, N. Cox, J. Messinger, W. Lubitz, S. DeBeer, F. Neese and D. A. Pantazis, *Chem. Sci.*, 2015, **6**, 1676-1695; (f) H. B. Lee, A. A. Shiau, P. H. Oyala, D. A. Marchiori, S. Gul, R. Chatterjee, J. Yano, R. D. Britt and T. Agapie, *J. Am. Chem. Soc.*, 2018, **140**, 17175–17187.

3 (a) C. Choe, L. Yang, Z. Lv, W. Mo, Z. Chen, G. Li and G. Yin, *Dalton Trans.*, 2015, **44**, 9182-9192; (b) C. Palopoli, J. Ferreyra, A. Conte-Daban, M. Richezzi, A. Foi, F. Doctorovich, E. Anxolabéhère-Mallart, C. Hureau and S. R. Signorella, *ACS Omega*, 2019, **4**, 48–57; (c) M. M. Whittaker, C. A. Ekberg, R. A. Edwards, E. N. Baker, G. B. Jameson and J. W. Whittaker, *J. Phys. Chem. B*, 1998, **102**, 4668–4677; (d) R. O. Costa, S. S. Ferreira, C. A. Pereira, J. R. Harmer, C. J. Noble, G. Schenk, R. W. A. Franco, J. A. L. C. Resende, P. Comba, A. E. Roberts, C. Fernandes and A. Horn Jr, *Front. Chem*., 2018, **6**, 491.

4 (a) R. Yan-Wei, L. Jun, Z. Feng-Xing, Z. Jin-Hua and G. Hui, *Chin. J. Chem*., 2005, **23**, 418-420; (b) K. Wieghardt, *Angew. Chem. Int. Ed. Engl.*, 1989, **28**, 1153-1172; (c) A. M. Magherusan, A. Zhou, E. R. Farquhar, M. García-Melchor, B. Twamley, L. Que Jr. and A. R. McDonald, *Angew. Chem. Int. Ed.*, 2018, **57**, 918-922.

5 (a) G. Berggren, P. Huang, L. Eriksson, S. Styring, M. F. Anderlund and A. Thapper, *Dalton Trans.*, 2010, **39**, 11035-11044; (b) M. M. Grush, J. Chen, T. L. Stemmler, S. J. George, C. Y. Ralston, R. T. Stibrany, A. Gelasco, G. Christou, S. M. Gorun, J. E. Penner-Hahn and S. P. Cramer, *J. Am. Chem. Soc.*, 1996, **118**, 65-69; (c) P. Karsten, A. Neves, A. J. Bortoluzzi, J. Strähle and C. Maichle-Mössmer, *Inorg. Chem. Commun*., 2002, **5**, 434-438; (d) U. Bossek, M. Saher, T. Weyhermüller and K. Wieghardt, *J. Chem. Soc., Chem. Commun.*, 1992, 1780-1782; (e) I. Michaud-Soret, L. Jacquamet, N. Debaecker-Petit, L. Le Pape, V. V. Barynin and J.-M. Latour, *Inorg. Chem.*, 1998, **37**, 3874-3876.

6 (a) *Mixed Valency Systems: Applications in Chemistry, Physics and Biology*, ed. K. Prassides, Springer Netherlands, Dordrecht, The Netherlands, 1991; (b) R. J. Pace, L. Jin and R. Stranger, *Dalton Trans.*, 2012, **41**, 11145-11160; (c) D. P. Kessissoglou, *Coord. Chem. Rev*., 1999, **185–186**, 837-858; (d) M. Orio, D. A. Pantazis, T. Petrenko and F. Neese, *Inorg. Chem.*, 2009, **48**, 7251–7260; (e) P. Franz, C. Ambrus, A. Hauser, D. Chernyshov, M. Hostettler, J. Hauser, L. Keller, K. Krämer, H. Stoeckli-Evans, P. Pattison, H.-B. Bürgi and S. Decurtins, *J. Am. Chem. Soc.*, 2004, **126**, 16472–16477.

7 (a) H. Yoon, Y.-M. Lee, X. Wu, K.-B. Cho, R. Sarangi, W. Nam and S. Fukuzumi, *J. Am. Chem. Soc.*, 2013, **135**, 9186–9194; (b) O. A. Babich and E. S. Gould, *Inorg. Chem.,* 2004, **43**, 1779–1783; (c) S. Fukuzumi, H. Kotani, K. A. Prokop and D. P. Goldberg, *J. Am. Chem. Soc.*, 2011, **133**, 1859–1869; (d) T. Kurahashi, *Inorg. Chem.*, 2015, **54**, 8356–8366; (e) S. Fukuzumi, *Dalton Trans.*, 2015, **44**, 6696-6705.

8 (a) C.-C. Wu, S. Datta, W. Wernsdorfer, G.-H. Lee, S. Hill and E.-C. Yang, *Dalton Trans.*, 2010, **39**, 10160-10168; (b) N. Shaikh, A. Panja, S. Goswami, P. Banerjee, P. Vojtíšek, Y.-Z. Zhang, G. Su and S. Gao, *Inorg. Chem.*, 2004, **43**, 849–851; (c) Y. Zhang, J.-J. Zhang, A.-Q. Jia, Z.-F. Xin and Q.-F. Zhang, *J. Cluster Sci.*, 2018, **29**, 1345-1352; (d) A. M. Ako, V. Mereacre, I. J. Hewitt, R. Clérac, L. Lecren, C. E. Anson and A. K. Powell, *J. Mater. Chem.*, 2006, **16**, 2579-2586; (e) P.-H. Lin, S. Gorelsky, D. Savard, T. J. Burchell, W. Wernsdorfer, R. Clérac and M. Murugesu, *Dalton Trans.*, 2010, **39**, 7650-7658; (f) A. Arauzo, E. Bartolomé, A. C. Benniston, S. Melnic, S. Shova, J. Luzón, P. J. Alonso, A.-L. Barra and J. Bartolomé, *Dalton Trans.*, 2017, **46**, 720-732.

9 (a) D. Gatteschi and R. Sessoli, *Angew. Chem. Int. Ed.*, 2003, 42, 268-297; (b) S. Shova, A. Vlad, M. Cazacu, J. Krzystek, I. Bucinsky, M. Breza, D. Darvasiová, P. Rapta, J. Cano, J. Telser and V. B. Arion, *Dalton Trans*., 2017, **46**, 11817-11829; (c) M. Sigrist, P. L. W. Tregenna-Piggott, K. S. Pedersen, M. A. Sørensen, A.-L. Barra, J. Hauser, S.-X. Liu, S. Decurtins, H. Mutka and J. Bendix, *Eur. J. Inorg. Chem*., 2015, 2683-2689; (d) S. Shova, A. Vlad, M. Cazacu, J. Krzystek, A. Ozarowski, M. Malček, L. Bucinsky, P. Rapta, J. Cano, J. Telser and V. B. Arion, *Dalton Trans*., 2019, **48**, 5909-5922; (e) S. Dutta and R. Ch. Deka, *Comput. Theor. Chem*., 2015, **1072**, 1-6.

10 (a) M. A. Halcrow, *Chem. Soc. Rev.*, 2013, **42**, 1784-1795; (b) G. Christou, *Polyhedron*, 2005, **24**, 2065-2075; (c) A. J. Fitzpatrick, S. Stepanovic, H. Müller-Bunz, M. A. Gruden-Pavlović, P. García-Fernández and G. G. Morgan, *Dalton Trans.*, 2016, **45**, 6702-6708; (d) R. Sessoli, D. Gatteschi, A. Caneschi and M. A. Novak, *Nature*, 1993, **365**, 141-143; (e) S. Spirkl, M. Grzywa and D. Volkmer, *Dalton Trans.*, 2018, **47**, 8779-8786; (f) C. Murray, B. Gildea, H. Müller-Bunz, C. J. Harding and G. G. Morgan, *Dalton Trans.*, 2012, **41**, 14487-14489; (g) G. A. Craig, J. J. Marbey, S. Hill, O. Roubeau, S. Parsons and M. Murrie, *Inorg. Chem*., 2015, **54**, 13-15.

11 (a) K. S. Pedersen, J. Dreiser, H. Weihe, R. Sibille, H. V. Johannesen, M. A. Sørensen, B. E. Nielsen, M. Sigrist, H. Mutka, S. Rols, J. Bendix and S. Piligkos, *Inorg. Chem*., 2015, **54**, 7600–7606; (b) C. Beghidja, G. Rogez and R. Welter, *New J. Chem*., 2007, **31**, 1403–1406; (c) C.-M. Liu, D.-Q. Zhang and D.-B. Zhu, *Chem. Asian J*., 2011, **6**, 74–77; (d) L. A. Kushch, V. D. Sasnovskaya, A. I. Dmitriev, E. B. Yagubskii, O. V. Koplak, L. V. Zorina and D. W. Boukhvalov, *Dalton Trans.*, 2012, **41**, 13747-13754.

12 (a) R. Bikas, H. Hosseini-Monfared, G. Zoppellaro, R. Herchel, J. Tucek, A. M. Owczarzak, M. Kubicki and R. Zboril, *Dalton Trans*., 2013, **42**, 2803-2812; (b) L. Botana, J. Ruiz, A. J. Mota, A. Rodríguez-Diéguez, J. M. Seco, I. Oyarzabal and E. Colacio, *Dalton Trans.*, 2014, **43**, 13509-13524; (c) I. Oyarzabal, J. Ruiz, A. J. Mota, A. Rodríguez-Diéguez, J. M. Seco and E. Colacio, *Dalton Trans.*, 2015, **44**, 6825-6838; (d) R. Bikas, F. Ajormal, M. Emami, J. Sanchiz, N. Noshiranzadeh and A. Kozakiewicz, *Polyhedron*, 2019, **162**, 20-29.

13 (a) W.-H. Zhu, S. Li, C. Gao, X. Xiong, Y. Zhang, L. Liu, A. K. Powell and S. Gao, *Dalton Trans.*, 2016, **45**, 4614-4621; (b) S. Saha, N. Biswas, A. Sasmal, C. J. Gómez-García, E. Garribba, A. Bauza, A. Frontera, G. Pilet, G. M. Rosair, S. Mitra and C. R. Choudhury, *Dalton Trans.*, 2018, **47**, 16102-16118; (c) M. N. Akhtar, Y. Lan, M. A. AlDamen, Y.-Z. Zheng, C. E. Anson and A. K. Powell, *Dalton Trans.*, 2018, **47**, 3485-3495; (d) J. P. Costes, S. Titos-Padilla, I. Oyarzabal, T. Gupta, C. Duhayon, G. Rajaraman and E. Colacio, *Inorg. Chem.*, 2016, **55**, 4428–4440; (e) A. K. Mondal, S. Goswami and S. Konar, *Dalton Trans.*, 2015, **44**, 5086-5094; (f) K. Zhang, G.-P. Li, V. Montigaud, O. Cador, B. Le Guennic, J. Tang and Y.-Y. Wang, *Dalton Trans.*, 2019, **48**, 2135-2141.

14 (a) V. Hoeke, M. Heidemeier, E. Krickemeyer, A. Stammler, H. Bögge, J. Schnack and T. Glaser, *Dalton Trans.*, 2012, **41**, 12942-12959; (b) J. Pasán, J. Sanchiz, F. Lloret, M. Julve and C. Ruiz-Pérez, *CrystEngComm*, 2018, **20**, 7464-7472; (c) K. R. McClain, C. A. Gould, K. Chakarawet, S. J. Teat, T. J. Groshens, J. R. Long and B. G. Harvey, *Chem. Sci*., 2018, **9**, 8492-8503; (d) T.-T. Wang, M. Ren, S.-S. Bao, B. Liu, L. Pi, Z.-S. Cai, Z.-H. Zheng, Z.-L. Xu and L.-M. Zheng, *Inorg. Chem*., 2014, **53**, 3117–3125.

15 (a) H. Y. Huang, Z. Y. Chen, R.-P. Wang, F. M. F. de Groot, W. B. Wu, J. Okamoto, A. Chainani, A. Singh, Z.-Y. Li, J.-S. Zhou, H.-T. Jeng, G. Y. Guo, J.-G. Park, L. H. Tjeng, C. T. Chen and D. J. Huang, *Nat. Commun.,* 2017, **8**, 15929; (b) W.-W. Liu, D. Wang, Z. Wang, J. Deng, W.-M. Lau and Y. Zhang, *Phys. Chem. Chem. Phys.*, 2017, **19**, 6481-6486; (c) M. H. Abdellatif,

C. Innocenti, I. Liakos, A. Scarpellini, S. Marras and M. Salerno, *J. Magn. Magn. Mater.*, 2017, **424**, 402-409; (d) M. L. Baker, S. Piligkos, A. Bianchi, S. Carretta, D. Collison, J. J. W. McDouall, E. J. L. McInnes, H. Mutka, G. A. Timco, F. Tuna, P. Vadivelu, H. Weihe, H. U. Güdel and R. E. P. Winpenny, *Dalton Trans.*, 2011, **40**, 8533-8539.

16 (a) B. S. Tsukerblat, M. I. Belinskii and B. Y. Kuyavskaya, *Inorg. Chem.*, 1983, **22**, 995–997; (b) H. Zhao, C. P. Berlinguette, J. Bacsa, S. E. Tichy and K. R. Dunbar, *J. Cluster Sci.,* 2003, **14**, 235-252.

17 (a) R. T. Conley, *Infrared Spectroscopy*, Allyn & Bacon, Boston MA, USA, 1966; (b) K. Nakamoto, *Infrared and Raman Spectra of Inorganic and Coordination Compounds*, 6th Ed., John Wiley & Sons, Hoboken NJ, USA, 2009; (c) R. Bikas, P. Aleshkevych, H. Hosseini-Monfared, J. Sanchiz, R. Szymczak and T. Lis, *Dalton Trans.,* 2015, **44**, 1782–1789; (d) R. Bikas, M. Emami, K. Ślepokura and N. Noshiranzadeh, *New J. Chem.,* 2017, **41**, 9710–9717; (e) M. Ghorbanloo, S. Jafari, R. Bikas, M. S. Krawczyk and T. Lis, *Inorg. Chim. Acta*, 2017, **455**, 15–24; (f) R. Bikas, V. Lippolis, N. Noshiranzadeh, H. Farzaneh-Bonab, A. J. Blake, M. Siczek, H. Hosseini-Monfared and T. Lis, *Eur. J. Inorg. Chem.*, 2017, 999-1006.

18 (a) N. Noshiranzadeh, M. Emami, R. Bikas and A. Kozakiewicz, *New J. Chem.,* 2017, **41**, 2658-2667; (b) L. Mandal, S. Mandal and S. Mohanta, *New J. Chem.*, 2017, **41**, 4689-4701; (c) F. A. Afkhami, G. Mahmoudi, A. V. Gurbanov, F. I. Zubkov, F. Qu, A. Gupta and D. A. Safin, *Dalton Trans.*, 2017, **46**, 14888-14896; (d) F. Yu, M. Xiang, A.-H. Li, Y.-M. Zhang and B. Li, *CrystEngComm*, 2015, **17**, 1556-1563; (e) A. Das, K. Bhattacharya, L. K. Das, S. Giri and A. Ghosh, *Dalton Trans.*, 2018, **47**, 9385-9399; (f) H. Hosseini-Monfared, R. Bikas, M. Siczek, T. Lis, R. Szymczak and P. Aleshkevych, *Inorg. Chem. Commun*., 2015, **62**, 60-63.

19 (a) R. Bikas, H. Hosseini-Monfared, V. Vasylyeva, J. Sanchiz, J. Alonso, J. M. Barandiaran and C. Janiak, *Dalton Trans*., 2014, **43**, 11925–11935; (b) F. Dimiza, C. P. Raptopoulou, V. Psycharis, A. N. Papadopoulos and G. Psomas, *New J. Chem.*, 2018, **42**, 16666-16681; (c) F. Matyuska, A. Szorcsik, N. V. May, Á. Dancs, É. Kováts, A. Bényei and T. Gajda, *Dalton Trans.*, 2017, **46**, 8626-8642; (d) R. Bikas, R. Karimian, M. Siczek, S. Demeshko, H. Hosseini-Monfared and T. Lis, *Inorg. Chem. Commun*., 2016, **70**, 219-222; (e) R. Bikas, N. Noshiranzadeh. L. Sieroń. H. Hosseini-Monfared, J. M. Barandiaran, T. Lis and J. Alono, *Inorg. Chem. Commun*., 2016, **67**, 85-89.

20 (a) I. B. Bersuker, *The Jahn–Teller Effect*, Cambridge University Press, Cambridge, UK, 2006; (b) M.-M. Yu, Z.-H. Ni, C.-C. Zhao, A.-L. Cui and H.-Z. Kou, *Eur. J. Inorg. Chem.,* 2007, 5670-5676; (c) Z. Lu and C. Fan, *Inorg. Chem. Commun*., 2011, **14**, 1329-1332; (d) R. Bikas, V. Kuncser, J. Sanchiz, G. Schinteie, M. Siczek, H. Hosseini-Monfared and T. Lis, *Polyhedron*, 2018, **147**, 142-151; e) R. Çelenligil-Çetin, P. Paraskevopoulou, N. Lalioti, Y. Sanakis, R. J. Staples, N. P. Rath and P. Stavropoulos, *Inorg. Chem.,* 2008, **47**, 10998-11009.

21 K. Kambe, *J. Phys. Soc. Jpn*., 1950, **5**, 48–51.

22 E. Coronado, J. R. Galán-Mascarós, C. Giménez-Saiz, C. J. Gómez-García and C. Ruiz-Pérez, *Eur. J. Inorg. Chem*., 2003, 2290–2298.

23 (a) R. Bikas, H. Hosseini-Monfared, J. Sanchiz, M. Siczek and T. Lis, *RSC Adv.,* 2014, **4**, 36175–36182; (b) R. Davila, N. Farias, E. C. Sañudo, A. Vega, A. Escuer, M. Soler and J. Manzur, *New J. Chem*., **2016**, *40*, 6164–6170; (c) Q.-W. Xie, X. Chen, K.-Q. Hu, Y.-T. Wang, A.-L. Cui and H.-Z. Kou, *Polyhedron*, 2012, **38**, 213–217; (d) D. Mandal, P. B. Chatterjee, S. Bhattacharya, K.-Y. Choi, R. Clérac and M. Chaudhury, *Inorg. Chem*., 2009, **48**, 1826–1835; (e) M. Hirotsu, M. Kojima and Y. Yoshikawa, *Bull. Chem. Soc. Jpn*., 1997, **70**, 649–657.

View Article Online
DOI: 10.1039/C9DT01652J

24 N. F. Chilton, R. P. Anderson, L. D. Turner, A. Soncini and K. S. Murray, *J. Comput. Chem*., 2013, **34**, 1164–1175.

25 (a) R. Boča, *Coord. Chem. Rev*., 2004, **248**, 757–815; (b) J. Krzystek, A. Ozarowski and J. Telser, *Coord. Chem. Rev*., 2006, **250**, 2308–2324.

26 N. Noshiranzadeh, M. Emami, R. Bikas, J. Sanchiz, M. Otręba, P. Aleshkevych and T. Lis, *Polyhedron,* 2017, **122**, 194–202.

27 *CrysAlis*^{Pro} v40, Rigaku Oxford Diffraction, Oxford, UK, 2015.

28 O. V. Dolomanov, L. J. Bourhis, R. J. Gildea, J. A. K. Howard and H. Puschmann, *J. Appl. Crystallogr.,* 2009, **42***,* 339-341.

29 G. M. Sheldrick, *Acta Crystallogr. Sect. A*, 2008, **64**, 112-122.

30 M. J. Frisch, G. W. Trucks, H. B. Schlegel, G. E. Scuseria, M. A. Robb, J. R. Cheeseman, G. Scalmani, V. Barone, G. A. Petersson, H. Nakatsuji, X. Li, M. Caricato, A. Marenich, J. Bloino, B. G. Janesko, R. Gomperts, B. Mennucci, H. P. Hratchian, J. V. Ortiz, A. F. Izmaylov, J. L. Sonnenberg, D. Williams-Young, F. Ding, F. Lipparini, F. Egidi, J. Goings, B. Peng, A. Petrone, T. Henderson, D. Ranasinghe, V. G. Zakrzewski, J. Gao, N. Rega, G. Zheng, W. Liang, M. Hada, M. Ehara, K. Toyota, R. Fukuda, J. Hasegawa, M. Ishida, T. Nakajima, Y. Honda, O. Kitao, H. Nakai, T. Vreven, K. Throssell, J. A. Montgomery Jr., J. E. Peralta, F. Ogliaro, M. Bearpark, J. J. Heyd, E. Brothers, K. N. Kudin, V. N. Staroverov, T. Keith, R. Kobayashi, J. Normand, K. Raghavachari, A. Rendell, J. C. Burant, S. S. Iyengar, J. Tomasi, M. Cossi, J. M. Millam, M. Klene, C. Adamo, R. Cammi, J. W. Ochterski, R. L. Martin, K. Morokuma, O. Farkas, J. B. Foresman and D. J. Fox, *Gaussian 09*, Revision A.02, Gaussian, Inc., Wallingford CT, 2009.